Exploring dust formation in the episodic WCd system WR140

J. W. Eatson⋆ & J. M. Pittard
School of Physics and Astronomy, University of Leeds, Woodhouse Lane, Leeds LS2 9JT, UK

ABSTRACT

Key words: stars: Wolf-Rayet – methods: numerical – binaries: general

1 INTRODUCTION

The dynamics of massive stars in binary systems is a particularly fascinating subject. These incredibly violent phenomena are obscured behind vast clouds of outflowing stellar wind, the result of the most massive stars we know slowly tearing themselves asunder. Colliding wind binary (CWB) systems were first hypothesised to explain highly luminous and variable x-ray emission in systems such as V444 Cyg and γ^2 Vel (Prilutskii & Usov 1976). These extremely bright emissions were found to be due to stellar wind collision with shock velocities in the order of $10^3\,\mathrm{km\,s^{-1}}$. The variability in x-ray emission can be explained if the phenomena occurs due to the orbit of a binary system, such as the Wind Collision Region (WCR) being occluded by the outflowing stellar wind, being occluded by the stars themselves. The system can also have an eccentric orbit, reducing the shock strength as the orbital separation, d_{sep}, varies. Despite this dust-hostile environment, CWB systems containing a Wolf-Rayet carbon phase star (WC) have been observed producing copious quantities of dust (so-called WCd systems). These systems typically convert around 1% of the stellar wind into dust a short time after wind collision; in more prolific systems such as WR104 up to 36% of the Wolf-Rayet (WR) outflow is converted into dust (Lau et al. 2020). This corresponds to dust production rates on the order of $10^{-6}\,\mathrm{M_\odot\,yr^{-1}}$, rivalling other profuse dust producing phenomena such as AGB stars.

WCd systems can sub-categorised further, into persistent, variable and episodic dust forming systems. Persistent systems, such as WR104 (Tuthill et al. 1999), produce dust at a constant rate, and as such produce extreme quantities of dust, as well as well-defined pinwheel patterns if the system is viewed face-on. Episodic systems, meanwhile, only produce dust for a limited period before entering a period of dormancy; this pattern is cyclical, and is predictably periodic. A good example of such an episodic system is WR140, the subject of this paper (Williams et al. 1990). Variable systems have some characteristics of these two sub-types, having a distinct variability without a period of dust producing dormancy, such as WR98a (Monnier et al. 1999). Whether a system is persistent, variable or episodic is based on the systems orbital eccentricity, highly eccentric systems appear to form episodic systems, with the "active" dust production period occurring immediately after periastron passage, and

a relatively short time thereafter. Meanwhile, persistent and variable systems have been observed to have more circular orbits, suggesting that the effect of a change in system separation distance, d_{sep}, has a role in dust formation. The initial mechanism behind dust formation is not well understood, whilst nascent amorphous carbon dust grain cores can form condense within the photosphere of WC7-9 stars, these grain cores would be vaporised by UV flux of both stars. However, within the WCR these grains appear to flourish, observations of these systems show that infrared excess in wavelengths associated with amorphous grains is detected almost exclusively within the post-shock WCR (Soulain et al. 2018). Observations also indicate that dust formation occurs rapidly and close to the system, this requires strong radiative cooling for the immediate-post shock temperature to reduce from $\sim 10^8$ K to $\sim 10^4$ K (Williams et al. 1987, 1990). As such, dust formation appears to be encouraged in the WCR through a multitude of factors:

• The high density of the post-shock WCR results in a high collision rate between carbon atoms and dust grains.

• The WCR shields nascent dust grains from the bulk of the UV emission from the stars.

• The rapid cooling in the immediate post-shock environment reduces gas-grain sputtering.

• Strong radiative cooling drives the formation of thermal instabilities, which produces clumps of cool, high density gas where dust can rapidly grow.

This dust formation can also be influenced by orbital separation, velocity shear and momentum ratio imbalance between the winds, producing variability on the timescale of a single orbit, or $t_{\mathrm{dyn}} \ll P$.

WCd systems are comparatively rare, out of 106 confirmed systems with a WR binary, only 9 are categorised as episodic WCd systems (Table 1). As these systems have a typical distance on the order of $1 - 10$ kpc, this makes observation of WCds difficult. Whilst these systems can be observed and the dusty WCR can be resolved, observation of the innermost, immediate post-shock dust forming region is not possible at this distance. As such, numerical simulation is necessary to determine dust formation in WCd systems, a contemporary example of such simulations is Hendrix et al. (2016), though simulation of the evolution of dust grains through cooling, growth and sputtering was not performed. In this paper we present a numerical simulation of the archetypal episodic WCd system WR140 with a co-moving dust model simulating grain growth and sputtering

⋆ E-mail: py13je@leeds.ac.uk

	Persistent		Variable		Episodic	
	Total	Example	Total	Example	Total	Example
WC4	1	WR19	0	—	0	—
WC5	0	—	0	—	1	WR47C
WC6	1	WR124-10	0	—	0	—
WC7	3	WR102-22	0	—	4	WR140
WC8	6	WR13	1	WR48a	3	WR122-14
WC9	45	WR104	6	WR98a	1	WR75-11
Total	56		7		9	

Table 1. Number of WCd systems with a known spectral type and dust formation type from the Galactic Wolf Rayet Catalogue (Rosslowe & Crowther 2015). Systems with uncertain spectral types not included, while systems labelled "d" are included within the "persistent" category for their associated spectral type.

through gas-grain collisions. This simulation covers a temporal slice of the orbit of WR140 from phase $\Phi = 0.95$ to $\Phi = 1.10$, or the period immediately prior to and after periastron passage. We will discuss our methodology in Section 2, with a particular emphasis on our dust model in Subsection 2.2. Afterwards we will discuss the simulation and WR140 system parameters, as well as our data collection techniques in Section 3. Finally, we will discuss our results and conclude in Sections 4 and 5.

2 METHODOLOGY

The periodic dust forming system WR140 was simulated using a fork of the Athena++ hydrodynamical code (Stone et al. 2020), a series of modifications were implemented to simulate binary system orbits, stellar wind outflows and dust evolution. These simulations were conducted in 3D in a Cartesian co-ordinate system. The code solves a Riemann problem at each cell interface to determine the time-averaged values at the zone interfaces, and then solves the equations of hydrodynamics:

$$\frac{\partial \rho}{\partial t} + \nabla \cdot (\rho \boldsymbol{u}) = 0, \tag{1a}$$

$$\frac{\partial \rho \boldsymbol{u}}{\partial t} + \nabla \cdot (\rho \boldsymbol{u} \boldsymbol{u} + P) = 0, \tag{1b}$$

$$\frac{\partial \rho \varepsilon}{\partial t} + \nabla \cdot [\boldsymbol{u}(\rho \varepsilon + P)] = \frac{dE_{\text{cool}}}{dt}, \tag{1c}$$

where ε is the total specific energy ($\varepsilon = \boldsymbol{u}^2/2 + e/\rho$), ρ is the gas density, e is the internal energy density, P is the gas pressure and u is the gas velocity. In order to simulate radiative losses, the parameter dE_{cool}/dt is included, which is the rate of energy loss rate per unit volume from the fluid due to gas and dust cooling.

Spatial reconstruction using a piecewise linear method was performed, while two strong stability Runge-Kutta methods were used for numerical integration, depending on the simulation stability. Several passive scalars are utilised to model wind mixing and dust evolution, the scalar values are transported by the fluid. For a given scalar species i, the scalar is advected through the scalar through the following equation:

$$\rho \frac{dC_i}{dt} = \frac{\partial}{\partial t}(\rho C_i) + \nabla \cdot (C_i \rho \mathbf{u}) = -\nabla \cdot \mathbf{Q}_i, \tag{2}$$

where $\mathbf{Q}_i$ is the diffusive flux density ($\mathbf{Q}_i = -\nu_{ps}\rho\nabla C_i$) and ν is the passive scalar diffusion coefficient (Stone et al. 2020).

Stellar winds are simulated by modifying the density, ρ_R, momentum, p_R, and energy, E_R in a small region around both stars. Winds

flow from this "remap" region at the stars wind terminal velocity, v^∞. Remap zone parameters are calculated with the formulae

$$\rho_R = \frac{\dot{M}}{4\pi r^2 v_\infty}, \tag{3a}$$

$$p_R = \rho_R v_r, \tag{3b}$$

$$E_R = \frac{P_R}{\gamma - 1} + \frac{1}{2}\rho_R v_\infty^2, \tag{3c}$$

where P_R is the cell pressure ($P_R = \rho_R k_B T_w / \mu m_H$), T_w is the wind temperature, μ is the mean molecular mass, m_H is the mass of a hydrogen atom, v_R is the wind velocity as it flows radially from the center of the "remap zone" and r is the distance from the current cell to the centre of the remap zone. This method produces radially out-flowing winds from the star with an expected density and velocity. This method is stable against numerical instability, while also allowing us to precisely control the winds.

Line driving and wind acceleration effects are not simulated; instead, winds are instantaneously accelerated to their terminal velocity. Additionally, influence on the fluid from either gravitational self-interaction or interaction with the stars gravity wells are not simulated, with the stellar winds assumed to be travelling far in excess of the system escape velocity.

Athena++ utilises Message Passing Interface (MPI) parallelism. The numerical problem is broken into blocks, which are distributed between processing nodes on a High Performance Compute (HPC) cluster. The block size is variable, but for this simulation a block size of $40 \times 40 \times 10$ cells in XYZ was found to be optimal. Adaptive Mesh Refinement was considered for this simulation, however a known issue with the Athena++ code prevented this from being possible. Passive scalars incorporated into the simulation were found to not be conserved along the interfaces between mesh blocks undergoing refinement, this meant that the simulation would rapidly exhibit unphysical behaviour (this bug is recorded as issue #365 on the Athena++ Github repository[1]). A ring of refined cells across the orbital path was considered, but the performance improvements of this method were found to be negligible and not worth pursuing, as the block based refinement method of Athena++ would result in significant redundant refinement. Instead, a static mesh is used, where the stars predicted orbit over the simulation is refined to the maximum level, with a gradual de-refinement away from this refinement region.

2.1 Radiative cooling

Cooling is simulated via the removal of energy from a cell at each time-step. A cooling rate, for radiative emission from the stellar wind, dE_g/dt, is calculated and integrated using a sub-stepping Euler method. The number of sub-steps is determined by the estimated cooling timescale of the cell. Cooling due to gas and plasma emission in the stellar winds are calculated via individual lookup tables from each wind. These lookup tables contain the normalised emissivity, $\Lambda_w(T)$ at a logarithmically spaced series of temperatures from 10^4 K to 10^9 K. The cooling rate is determined for a cell by calculating the cell temperature and estimating $\Lambda_w(T)$ using linear interpolation between the nearest emissivity values in the lookup table. The energy loss is then calculated through the equation:

---

[1] https://github.com/PrincetonUniversity/athena/issues/365

$$\frac{dE_g}{dt} = \left(\frac{\rho_g}{m_H}\right)^2 \Lambda_w(T), \tag{4}$$

where ρ_g is the gas density and m_H is the mass of hydrogen. The lookup table was generated by mixing a series of cooling curves from MEKAL simulations of elemental gasses. These curves were combined based on the elemental abundances in the WC and OB winds. To save calculation time, temperatures between 1×10^4 K $< T \leq 1.1 \times 10^4$ K are set to 1×10^4 K as they are assumed to be either rapidly cooling or a part of the stellar wind outside of the WCR. A minimum temperature of 10^4 K is defined by the simulation, is it is assumed that a radiating post-shock wind will tend to the temperature of the pre-shock wind, $T_{\text{final}} \rightarrow T_{\text{pre-shock}}$.

2.2 Dust model

In order to simulate dust evolution in WR140 a passive scalar dust model that simulates dust growth and destruction is included in the simulation. The dust model operates on passive scalars, and as such simulates dust that is co-moving with the stellar wind. Two scalars are used to describe dust in a cell, a, the grain radius in microns, and z, the grain dust-to-gas mass ratio

$$z = \frac{\rho_d}{\rho_g}, \tag{5}$$

where ρ_d is the dust density in the cell. A number of assumptions are made in this dust model; for instance, the dust grains in the model are spherical, with a uniform density. Dust grains are also assumed to have a single size in a region, as well as a constant number density. As such, this model does not simulate grain fracturing. Additional mechanisms for dust formation and destruction could also be implemented such as grain-grain agglomeration and photoevaporation. A multi-fluid model with drag force coupling could also be implemented, however this is beyond the scope of this paper.

Dust is grown through grain accretion using formulae described by (Spitzer 2008) where dust grains grow via low-velocity collisions with surrounding carbon atoms, causing them to accrete onto the surface of the dust grain. Carbon is removed from the gas, reducing the cell density, while the corresponding dust density increases. This ensures that mass is preserved in the simulation. Assuming a single average grain size the rate of change in the grain radius in a cell, da/dt, is given by the equation:

$$\frac{da}{dt} = \frac{\xi \rho_C w_C}{4 \rho_{gr}}, \tag{6}$$

where ξ is the grain sticking factor, ρ_C is the carbon density ($\rho_C = X_C \rho_g$), w_C is the Maxwell-Boltzmann RMS velocity for carbon ($w_C = \sqrt{3 k_B T / 12 m_H}$), k_B is the Boltzmann constant and ρ_{gr} is the grain bulk density. The rate of change in grain mass due to accretion, $dm_{gr,ac}/dt$, is calculated with the formulae:

$$\frac{dm_{gr,ac}}{dt} = 4\pi \rho_{gr} a^2 \frac{da}{dt} = \pi \xi \rho_C w_C a^2, \tag{7}$$

A bulk density approximating that of amorphous carbon grains ($\rho_{gr} = 3.0 \, \text{g cm}^{-3}$) is used for this simulation.

Dust destruction through gas-grain sputtering is calculated using the Draine & Salpeter (1979) prescription. Within a flow of number density n_g a dust grain of radius a has a grain lifespan, τ_{gr} of:

$$\tau_{gr} = \frac{a}{\dot{a}} \approx 3 \times 10^6 \frac{a}{n_g} \, \text{yr}. \tag{8}$$

This value is based on an average lifetime of carbon grains in an interstellar shock with a temperature of 1×10^6 K $\leq T \leq 3 \times 10^8$ K (Tielens et al. 1994; Dwek et al. 1996). The rate of change in the dust grain mass due to sputtering, $dm_{gr,sp}/dt$, can then be calculated with a similar formulae to the rate of change in grain mass due to accretion:

$$\frac{dm_{gr,sp}}{dt} = 4\pi \rho_{gr} a^2 \frac{da}{dt} = -4\pi \tau_{gr} n_g a^2. \tag{9}$$

Finally, the total rate of change in grain mass is calculated, the overall change in dust density is then calculated through the equation:

$$\frac{d\rho_d}{dt} = \left(\frac{dm_{gr,acc}}{dt} + \frac{dm_{gr,sp}}{dt}\right) n_d, \tag{10}$$

where n_d is the dust grain number density.

Cooling via emission of photons from dust grains is also included in this model. The rate of cooling is calculated using the uncharged grain case of the prescription described in Dwek & Werner (1981). Grains are collisionally excited by collisions with ions and electrons, causing them to radiate. Similarly to the gas/plasma emission model used, the emitted photons are not re-adsorbed by the WCR medium, causing energy to be removed from the simulation. This therefore makes the assumption that the WCR is optically thin to far-infrared photons, which is observationally correct (Monnier et al. 2007; Soulain et al. 2018; Callingham et al. 2019). The grain heating rate, H_{coll}, in erg s^{-1} for a dust grain is calculated with the formulae:

$$H = 1.26 \times 10^{-19} \frac{n_g}{A^{1/2}} a^2 (\mu m) T^{3/2} h(a, T), \tag{11}$$

where n_g is the gas number density, A is the mass of the incident particle in AMU, $a(\mu m)$ is the grain radius in microns, T is the temperature of the ambient gas, and $h(a, T)$ is the effective grain heating factor. Individual heating rates for hydrogen, helium, carbon, nitrogen and oxygen are calculated, in order to calculate the total ion collisional heating, H_{coll}:

$$H_{coll} = H_H + H_{He} + H_C + H_N + H_O. \tag{12}$$

The effective grain heating factor for each element is calculated via the equation:

$$h(a, T) = 1 - \left(1 + \frac{E^*}{2 k_B T}\right) e^{-E^*/k_B T}, \tag{13}$$

where E^* is the critical energy required for the particle to penetrate the dust grain (Table 2). The rate of heating due to electron-grain collisions, H_{el}, is similar to Eq. 11. The grain heating factor for electron collisions, h_e, is calculated via an approximation rather than the exact calculation in the case of baryonic matter. This approximation is performed as a complex integration for every cell and cooling step would need to be performed instead, which was found to take up $> 90\%$ of the processing time per cell. h_e is estimated through the following conditions:

$$\begin{aligned} h_e(x^*) &= 1, & x^* > 4.5, \\ &= 0.37 x^{*0.62}, & x^* > 1.5, \\ &= 0.27 x^{*1.50}, & \text{otherwise}, \end{aligned} \tag{14}$$

Particle	E^*
e^-	$23\,a^{2/3}\,(\mu m)$
H	$133\,a\,(\mu m)$
He	$222\,a\,(\mu m)$
C	$665\,a\,(\mu m)$
N	$665\,a\,(\mu m)$
O	$665\,a\,(\mu m)$

Table 2. Grain critical energy, E^*, for a dust grain of a in μm for electrons, e^-, as well as the elements considered for grain cooling. The values for carbon, oxygen and nitrogen are identical.

where $x^* = 2.71 \times 10^8 a^{2/3} (\mu m)/T$. This approximation differs from the integration method by less than 8% while being 3 orders of magnitude faster. Excitation due to grain-grain collisions were not modelled, due to the limitations of the passive scalar model. In order to calculate the change in energy due to dust cooling, we find the radiative emissivity for dust, $\Lambda_d(T, a)$, to be

$$\Lambda(T, a) = \frac{H_{coll} + H_{el}}{n_H}, \tag{15}$$

where n_H is the number density of hydrogen in the gas. The energy loss rate from dust cooling, dE_d/dt, then calculated with the equation:

$$\frac{dE_d}{dt} = n_T n_d \Lambda_d(T, a), \tag{16}$$

and added to the gas/plasma energy loss rate, such that the total energy loss rate is:

$$\frac{dE_{cool}}{dt} = \frac{dE_g}{dt} + \frac{dE_d}{dt}. \tag{17}$$

3 SYSTEM PARAMETERS

The authors of this paper have previously simulated WCd systems in the form of a parameter space exploration, in order to discern which wind and orbital parameters are influential on these systems dust formation rates. It was determined that the primary factors of dust formation in a WCd system were the mass loss rates, $\dot{M}$, and wind terminal velocities, v^∞, for each star, as well as the orbital separation, d_{sep}. In particular, it was found that imbalances between the wind velocity produced Kelvin-Helmholtz (KH) instabilities due to a shear in the winds. Slower winds were found to be more radiative in the post-shock WCR flow, cooling to temperatures suitable for dust formation, this was found to influence the dust formation rate by as much as six orders magnitude through a factor of four variation of the WR wind terminal velocity. The authors also found that increasing d_{sep} significantly reduced the dust production rate, due to less intensive shocks as the out-flowing winds became less dense with distance. In the case of WCd systems with eccentric orbits, the separation distance can vary significantly. In the case of WR140, d_{sep} varies by a factor of 18 from apastron to periastron, which was hypothesised to be the primary cause of dust production variability within episodic systems. As $\dot{M}$ does not vary significantly on the orbital timescale of these systems, this is not expected to impact the dust formation rate in episodic systems, while the wind velocity can diverge somewhat due to radiative inhibition and orbital motion.

In order to understand the structure and dynamics of the CWB system we must define some important parameters, such as the wind momentum ratio, η, which is defined as:

$$\eta = \frac{\dot{M}_{OB} v_{OB}^\infty}{\dot{M}_{WR} v_{WR}^\infty}. \tag{18}$$

As η decreases we find that the wind becomes more imbalanced, in the case of WR+OB CWB systems we find that the WR stars wind typically dominates the WCR. Assuming that there is no radiative inhibition (Stevens & Pollock 1994) or radiative braking (Gayley et al. 1997), we can approximate the WCR to a conical region with an opening angle:

$$\theta_c \simeq 2.1 \left(1 - \frac{\eta^{2/5}}{4}\right) \eta^{-1/3} \quad \text{for } 10^{-4} \le \eta \le 1, \tag{19}$$

to a relatively high degree of accuracy (Eichler & Usov 1993). Another important value for determining the evolution of a CWB system is the cooling parameter, χ, which is the ratio of the time taken for the shocked wind to completely cool to the time taken for the wind to escape the shock region:

$$\chi = \frac{t_{cool}}{t_{esc}} \approx \frac{v_8^4 d_{12}}{\dot{M}_{-7}}, \tag{20}$$

where v_8 is the wind terminal velocity in units of $10^8 \, \text{cm s}^{-1}$, d_{12} is the separation distance in units of 10^{12} cm and $\dot{M}_{-7}$ is the wind mass loss rate in units of $10^{-7} \, M_\odot \, \text{yr}^{-1}$ (Stevens et al. 1992). As χ decreases, the structure of the WCR becomes more influenced by radiative instabilities, and has a post-shock temperature approaching the initial wind temperature. If $\chi < 1$, the WCR is completely dominated by instabilities, while if $\chi \gg 1$, the system behaves adiabatically. If the WCR is highly radiative the post-shock compression can be significantly greater than the adiabatic limit of $\rho_{post-shock} = 4\rho_{pre-shock}$, which facilitates dust production. Finally, we define a maximum dust production rate of the system, $\dot{M}_{d,max}$, assuming a 100% conversion rate of WR wind in the WCR into dust. The fraction of the WR wind that is passed through the WCR is given by the equation:

$$f_{WR} = \frac{1 - \cos(\theta_{WR})}{2}, \tag{21}$$

where θ_{WR} is the opening angle of the WR shock front ($\theta_{WR} \approx 2 \tan^{-1}(\eta^{1/3}) + \pi/9$). $\dot{M}_{d,max}$ is then calculated with the formulae:

$$\dot{M}_{d,max} = \dot{M}_{WR} X_{C,WR} f_{WR}, \tag{22}$$

where X_C is the carbon mass fraction in the WR star (Pittard & Dawson 2018).

3.1 WR140 parameters

WR140 was simulated in this paper as it is an archetypical example of an episodic WCd system. THe system has an extremely eccentric orbit, which significantly effects the cooling parameter as the orbit progresses, and is also observed in detail and orbits face-on relative to the Earth. Though this simulation does not calculate wind acceleration due to radiative line driving, both stellar winds are expected to be accelerated to close to their terminal wind velocities (Lamers & Cassinelli 1999). However, this discrepancy should be noted when considering the results of this paper.

Recent improved estimations of the orbital parameters of WR140 by Thomas et al. (2021) were used to calculate the orbital path for these simulations, while the mass loss rate, and the wind terminal

Parameter	Value	Citation
M_{WR}	$10.31 \, M_\odot$	Thomas et al. (2021)
M_{OB}	$29.27 \, M_\odot$	Thomas et al. (2021)
P	$7.926 \, yr$	Thomas et al. (2021)
e	0.8993	Thomas et al. (2021)
$\dot{M}_{WR}$	$5.6 \times 10^{-5} \, M_\odot \, yr^{-1}$	Williams et al. (1990)
$\dot{M}_{OB}$	$1.6 \times 10^{-6} \, M_\odot \, yr^{-1}$	Williams et al. (1990)
v_{WR}^∞	$2.86 \times 10^3 \, km \, s^{-1}$	Williams et al. (1990)
v_{OB}^∞	$3.20 \times 10^3 \, km \, s^{-1}$	Williams et al. (1990)
η	0.031	Calculated
χ_{min}	2.69	Calculated

Table 3. The system parameters for the WR140 system as used in this paper. Citations for each parameter are provided.

Element	Solar	WC
X_H	0.705	0.000
X_{He}	0.275	0.546
X_C	0.003	0.400
X_N	0.001	0.000
X_O	0.010	0.050

Table 4. Abundances used for the OB and WR stars being simulated. Other elements are assumed trace when calculating dust emission (Williams et al. 2015).

velocity were derived from Williams et al. (1990) (Table 3). A typical wind composition for WC stars was assumed for the Wolf-Rayet star, while a solar abundance was assumed for the OB star (Table 4). The system orbit was calculated using a Keplerian orbital model with the two stars as point-masses.

3.2 Simulation parameters

A domain of $128 \times 128 \times 16$ AU was used for this simulation, with a coarse (0th level) simulation resolution of $400 \times 400 \times 50$ in the XYZ domain. The simulation has 4 refinement levels, corresponding to an effective resolution of $6400 \times 6400 \times 800$ cells and a cell size of 0.02^3 AU. At periastron passage this results in ~ 80 cells separating the stars, which was found to be enough to adequately resolve the WCR. This simulation has an XYZ aspect ratio of 8:8:1 in order to reduce processing time, as the bulk of dust formation was expected to occur a short distance from the WCR. Due to computing limitations, a complete orbit could not be completed without AMR, instead, a section of the systems orbit, corresponding to an orbital phase of $0.95 \leq \Phi \leq 1.10$ was simulated (Fig. 1). This represents a period of approximately 1.2 years of the systems orbit, and the period where much of the dust forms, prior to and shortly after periastron passage (Crowther 2003). Fig. 2 shows the orbital path overlaid onto the statically refined numerical grid, the area of maximum refinement is around the orbital paths of the stars from $0.94 \leq \Phi \leq 1.11$, in order to ensure that the stars are maximally refined. If the stars leave the regions that are refined to either the 3rd or 4th level unphysical behaviour with regards to wind mapping and dust formation occur, as such the simulation is halted when $\Phi = 1.10$. The simulation was run with two different numerical integrators, a 3rd order accurate Runge-Kutta integrator, `rk3`, and a 4th order accurate, 5-stage, 3 storage register strong stability preserving Runge-Kutta integrator, `ssprk5_4` (Ruuth & Spiteri 2005). The `ssprk5_4` integrator was found to be approximately 60% slower, but markedly more stable. Prior to periastron passage the `rk3` integrator was used for its speed, but increasing numerical instability as the stars grew closer resulted in this proving untenable, and was switched to `ssprk5_4`.
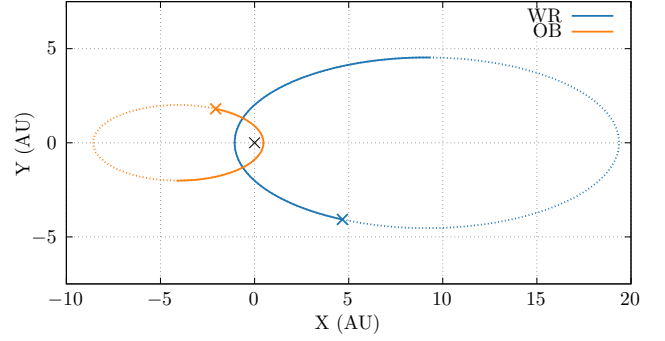
Figure 1. Simulation orbital trajectories of the WC7 and O5 stars in WR140. The solid lines represent the orbital phase being simulated, corresponding to $0.95 \leq \Phi \leq 1.10$, while the dashed lines represent the full orbital trajectory. The starting position for each star and the orbital barycentre at (0,0) have been annotated.

Over periastron passage the average time-step was found to reduce by an order of magnitude, resulting in a corresponding increase to simulation time. At the most numerically complex portion of the simulation, a Courant number of $C = 0.04$ had to be used instead of the initial value of $C = 0.15$, in order to preserve numerical stability. As the simulation moved past periastron the Courant number was increased every 24 hours of wall time, until C returned to the initial value. The simulation was conducted on the ARC4 HPC cluster at the University of Leeds with 128 cores. The code was compiled using the Intel `ICPC` compiler using `AVX512` optimisations and the Intel MPI library.

3.3 Data collection

Simulation data was exported as HDF5 files at regular time intervals. 3D meshes were collected every increment of $\delta\Phi = 1.5 \times 10^{-3}$, while 2D slices in the XY plane were collected every increment of $\delta\Phi = 1.5 \times 10^{-4}$. These HDF5 files contain the primitive variables of the simulation: gas density, ρ, gas pressure, P, and wind velocity components, v_x, v_y and v_z. These variables were then used to derive other variables such as temperature and energy. The scalars governing the dust properties were also stored for each cell: the dust-to-gas mass ratio, z, and the dust grain radius, a. The wind "colour", the proportion of gas from each star, was also stored. A value of 1.0 indicates a pure WR wind while 0.0 indicates a pure OB wind. The volume-weighted totals of all parameters of interest were also collected, such as the average values for z, a and the dust production rate within the WCR, $\dot{M}_d$. To calculate $\dot{M}_d$, a cell must be identified as being within the WCR, this was performed by comparing the cell density to the predicted density of a single wind with the wind parameters of the WC star in the system. Any cell with a density higher a certain threshold value was flagged as being within the WCR. the single-wind density, ρ_{SW}, was calculated using the equation:

$$\rho_{SW} = \frac{\dot{M}_{SW}}{4\pi r^2 v_{SW}^\infty}, \tag{23}$$

where r is the distance from the barycentre. This threshold value was set to $\rho_{thres} = 1.25\rho_{SW}$, which was found to accurately identify the WCR through thorough prior testing.
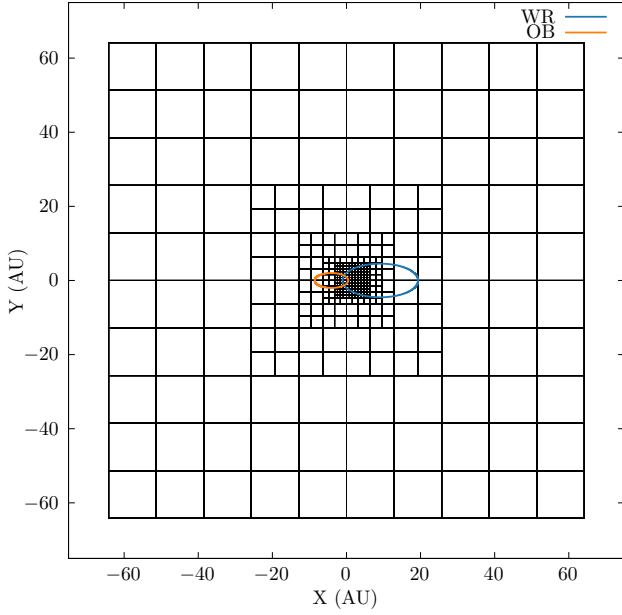
Figure 2. Numerical grid of the WR140 system simulation, static mesh refinement was used to increase the resolution around the orbital path from $0.95 \leq \Phi \leq 1.10$. The orbital path of both stars are overlaid onto this numerical grid. While the stars in the system can be within cells that are not fully refined, if there is insufficient resolution the stars begin to break down. As such the stars are typically in the 3rd or 4th level.

Parameter	Mean	Maximum
$\dot{M}_d$ ($M_\odot$ yr^{-1})	7.68×10^{-8}	1.24×10^{-6}
$\bar{a}$ (μm)	1.32×10^{-2}	1.44×10^{-2}
$\bar{z}$	3.98×10^{-4}	3.32×10^{-3}

**Table 5.** Advected scalar yields from the WR140 simulation.

4 RESULTS AND CONCLUSIONS

Dust production was found to be consistent with previous uses of this particular dust model. Dust production rates were found to be sensible, and significantly below the theoretical maximum dust formation rate, $\dot{M}_{d,max} \approx 4.8 \times 10^{-6} \, M_\odot \, yr^{-1}$. After an initial advection period lasting until $\Phi \approx 0.96$, the dust production rate rapidly increased as the stars approached periastron passage, peaking at $\Phi \sim 1.01$ (Fig. 3). This maximum dust production rate of $1.24 \times 10^{-6} \, M_\odot \, yr^{-1}$ is sensible, but incredibly prodigious, demonstrating a peak conversion efficiency of gas into dust of $\sim 26\%$ in the WCR and a total conversion efficiency of $\sim 2.2\%$ throughout the entire system. After reaching this maximum value, the dust production rate steadily decreases as the stars recede from each other. This is reflected in the overall dust mass of the simulation (Fig. 4), as well as in infrared observations of WR140, where the infrared emission from dust formation rapidly reaches a maximum value after periastron passage, and slowly relaxes to a minimum value. This asymmetry in the time-dependent change in infrared luminosity implies the existence of several factors for suppression and encouragement of dust formation than just the change in orbital separation distance. It should be noted that due to the small size of the simulation, the dust mass in the system will reduce quickly, as dust advects off of the numerical grid.

The evolution of dust in this system would result in the formation of an expanding cloud of dust every time the system passes perias-
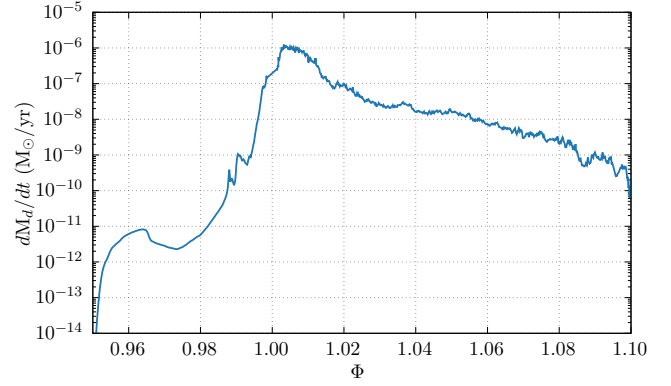

Figure 3. A graph of the dust production rate in the WCR over the orbital phase $0.95 \leq \Phi \leq 1.10$. The dust production rate sharply increases as the stars pass their closest approach. Afterwards, the dust production rate begins to falter and slow, due to weaker wind collision effects via the separation distance and radial velocity.
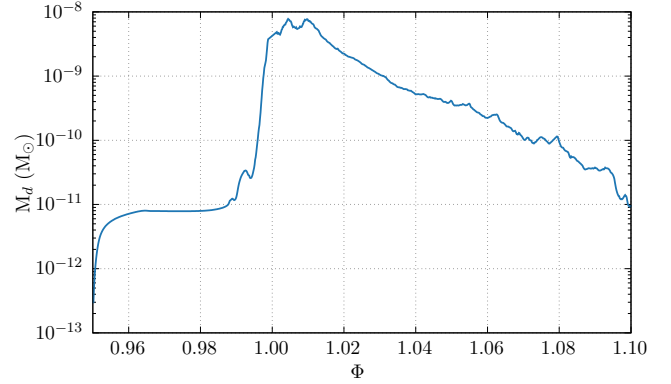

Figure 4. A graph of the overall dust mass in the simulation of WR140 over the orbital phase $0.95 \leq \Phi \leq 1.10$. The amount of dust quickly reduces after periastron due to a decreased dust formation rate (Fig. 3), as well as dust advecting off of the numerical grid.

tron, with no contiguous spiral pattern forming, due to the lengthy "dormant" period occurring shortly after periastron passage. This is consistent with observations of WR140, where these disconnected clouds are observed (Williams et al. 2009). We find an average dust production rate of $\dot{M}_d = 7.68 \times 10^{-8} \, M_\odot \, yr^{-1}$, and am change in the dust production rate by approximately five orders of magnitude over the course of the simulation. This fits our understanding of an episodic dust forming WCd system, with an extremely clear "active" period followed by a slow tapering off of dust production as the system approaches the "dormant" period. We can compare our results to the estimated dust yields from Lau et al. (2020), which found an average dust production rate of $\dot{M}_d = 8.11 \times 10^{-10} \, M_\odot \, yr^{-1}$. Our value for the dust-to-gas mass ratio within the system appears to be sensible, while our average dust production rate is significantly higher. This is due to the limited temporal sample of the simulation. We would find a significantly lower average dust production rate over the course of a full orbit due to more sampling of the system over the "dormant" period.
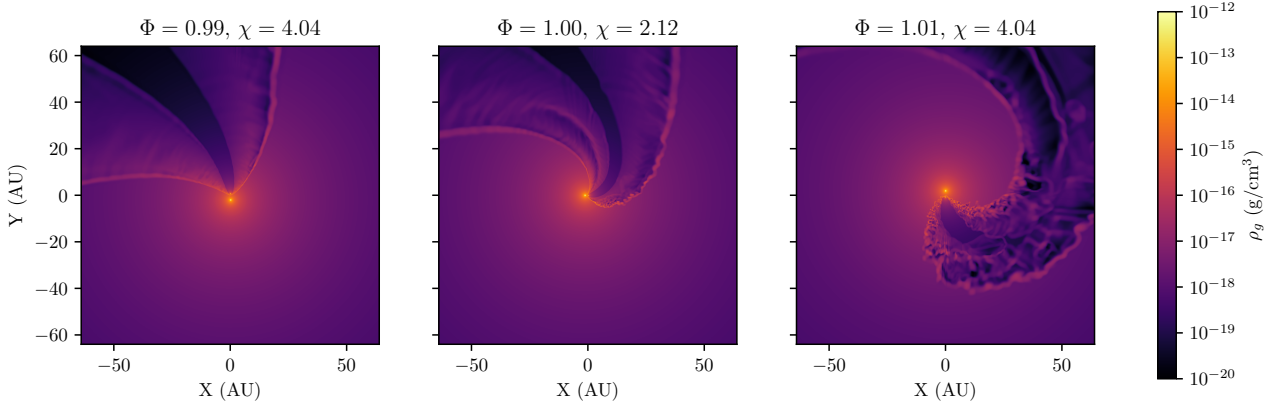
Figure 5. Gas density in a simulation of the WR140 system shortly before, during, and shortly after periastron. The simulation becomes rapidly dominated by instabilities a short while after periastron. However, these instabilities persist despite the system behaving adiabatically at a similar orbital separation distance prior to periastron. This suggests that the radiative behaviour of the post-shock WCR is due to multiple factors, other than dust a varying d_{sep}.
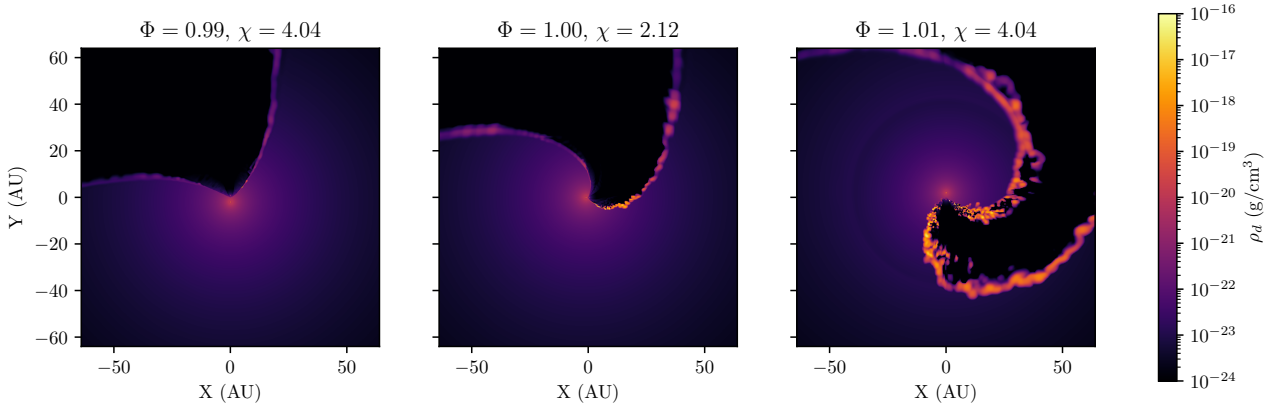
Figure 6. Dust density in a simulation of the WR140 system shortly before, during, and shortly after periastron. Dust formation occurs as a direct result of the formation of thermal and KH instabilities in the post-shock WCR.
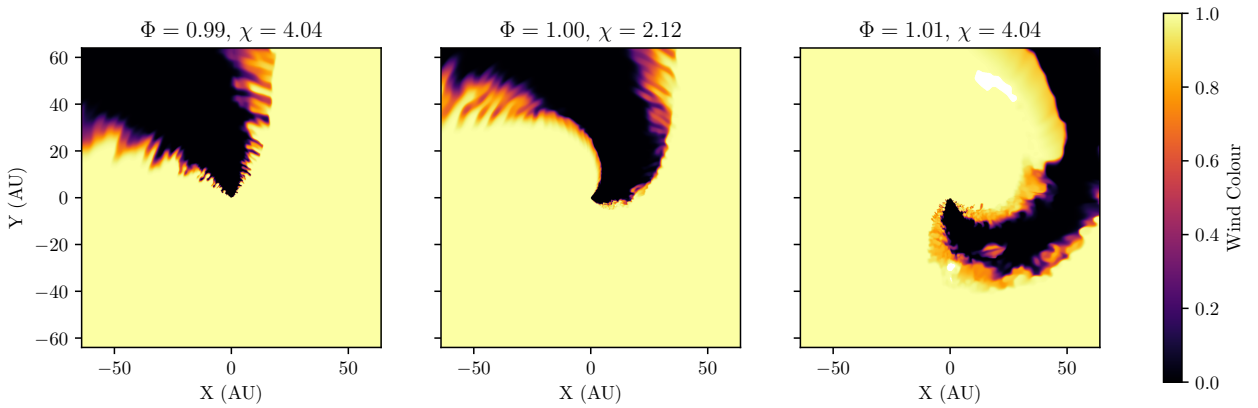
Figure 7. Wind "colour" in a simulation of the WR140 system shortly before, during, and shortly after periastron. With 1 representing a pure WR wind and 0 representing a pure OB wind. We find that the wind undergoes more mixing during and after periastron.

4.1 Instabilities

As can be seen in Fig. 5, after periastron passage the post-shock WCR region transitions from a smooth adiabatic wind to a highly radiative wind dominated by instabilities. As the WCR becomes increasingly dominated by instabilities, dust formation drastically increases, with the bulk of dust formation occurring within the high density regions produced by these instabilities. These clumpy pockets of gas do not exhibit significant dust formation beyond $\sim 20\,\mathrm{AU}$ from the simulation barycentre, with concentrations of dust remaining approximately constant (Fig. 6). By the end of the simulation at $\Phi = 1.10$, the WCR is still somewhat dominated by instabilities, with an elevated dust production rate even though the cooling parameter has increased significantly to $\chi = 19.7$, which would imply adiabatic behaviour. Whilst the dust formation rate has reduced significantly, there is still a significantly greater formation rate than at the start of the simulation (after advection). This suggests that the transition from radiative to adiabatic behaviour has a degree of latency, with instabilities still driving the structure of the WCR long after adiabatic flow should have been re-established. The amount of wind being mixed in the system is also significantly increased after periastron passage, which would be conducive to the formation of complex organic molecules on the surface of the dust grains (Fig. 7). Whilst research into this is out of the scope of the project, evolution of dust grains from WCd systems on longer time and length scales would be an enlightening avenue of research.

4.2 Influence of varying wind velocity on dust production

As we have previously discussed, varying the wind terminal velocity for both stars in a simulation can result in exponential changes in the dust production rate. This is theorised to be due to the increased influence of thermal instabilities through increased cooling in slower post-shock winds, as well as through KH instabilities driven through a wind velocity shear (if the wind terminal velocities are significantly different, see Stevens et al. 1992). Previous work on this subject considered systems with circular orbits, hence the orbital motion between the stars was persistent, and did not contribute to to a change in the wind velocities over the orbit of the system. However, in the case of a system with an eccentric orbit (such as WR140), we would find that both the outflow velocity for each wind - as well as the velocity ratio - would be markedly different over the systems orbit. As the stars approach periastron, the radial velocity, v_r for each star rapidly changes from a minimum value to a maximum, as the stars approach and then swing past one another. This sudden change in the stars radial velocity results in a rapid change in the velocity for both winds entering the collision region. This will influence the amount of radiative cooling in the post-shock wind, suppressing radiative cooling pre-periastron and inciting it post-periastron, altering the dust formation rates. While this change in wind velocity is relatively small, with the wind velocity varying by as much as 6% over the course of an orbit, this can still impact the cooling of the system. Due to χ being dependent on v^4, this effect can vary χ by as much as a factor of 1.26 in the case of WR140.

The rate of dust formation is also strongly governed by the presence of a large wind velocity ratio, Υ, where:

$$\Upsilon = v_{\mathrm{OB}}/v_{\mathrm{WR}}, \tag{24}$$

As the mass of each star is different, the change in velocity differs, causing an increased velocity ratio and therefore a stronger velocity shear. Previous research with dust models suggests that a strong
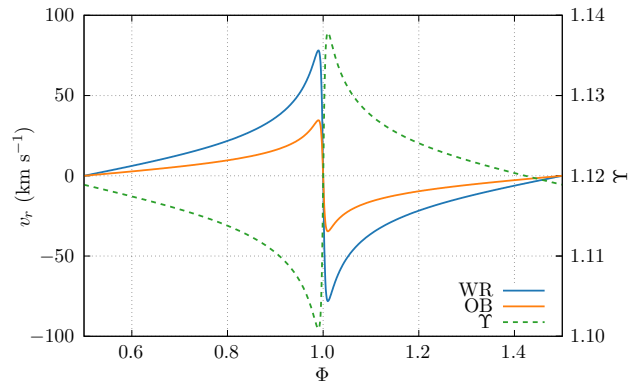

Figure 8. Radial velocity as a function of the orbital phase for the WR and OB stars in the WR140 system relative to the barycentre. As periastron passage occurs, the sudden inversion from approaching to receding can alter the wind velocity of the WR star by as much as $160\,\mathrm{km\,s^{-1}}$. Whilst this discrepancy is $\sim 6\%$ of the WR wind velocity, this can significantly increase dust production if the stars are receding from each other. The velocity shear, $v_{\mathrm{OB}}/v_{\mathrm{WR}}$, also sharply increases during periastron passage, peaking at the point of maximum dust formation.

velocity shear drives an increased dust formation rate. We find that the maximum change in velocity shear occurs at $\Phi = 1.01$, around the same time where the dust formation rate is at a maximum; this is consistent with our previous work (Fig. 8). Whilst this change in velocity shear would not significantly alter the dynamics of dust formation on its own, it may be another factor in explaining the increased dust formation of WR140 post-periastron, and explain why the system is still dominated by instabilities even after the system should be behaving adiabatically. However, this effect may also be decreased somewhat by the effect of radiative inhibition and braking on the winds. We find using a model estimating wind velocities using the Castor, Abbott & Klein (1975) model for radiative driving that the OB wind in particular is affected. Fig. 9 shows the wind velocities resultant from this model with CAK parameters for the WR and OB stars in WR140. We find that the wind velocity is approximately 84% of the expected velocity. This would decrease the velocity shear before and after periastron passage. The effect of radiative line driving from the CAK model is not considered in this simulation, and simulations considering this effect would have to be performed in order to study this further. This represents another interesting avenue of future research.

5 SUMMARY

Despite only simulating a limited section of the orbit of WR140, we have made a number of insights into the behaviour of the system. We find a significant degree of change in the dust formation rate as a direct consequence of the changing orbital separation of the system. This is related to the change in the behaviour of the post-shock WCR wind, which goes from a smooth adiabatic wind to a clumpy, high density wind dominated by instabilities ideal for dust formation. It is particularly interesting to note that the system does not revert to behaving adiabatically as quickly as it entered it. This suggests that the post-shock WCR condition of the system is dependent on additional factors, instead of being solely due to d_{sep}. One of the main factors on this delayed return to the adiabatic, "dormant" state is potentially due to the orbital motion of the stars themselves. As the stars ap-
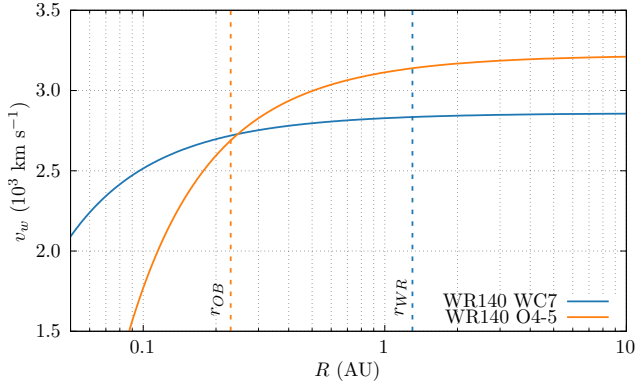
Figure 9. Graph of the wind velocity of the WC7 and O4-5 stars in the WR140 system as a function of distance from the stellar surface due to radiative line driving. The dashed lines represent the distance to the WCR at periastron for each star. During periastron passage the WC7 wind is travelling at approximately its terminal velocity before collision, while the O4-5 companions wind is travelling at ~ 84% of terminal velocity before coming into contact with the WCR. CAK parameters were estimated to be $k = 0.37$, $\alpha = 0.60$ for the O4-5 star and $k = 0.48$, $\alpha = 0.57$ for the WC7 star.

proach each other at periastron, the radial velocity of the stars adds velocity to the wind beyond the outflow velocity, resulting in higher wind collision velocities, which encourages adiabatic behaviour in the post-shock flow. The inverse is true as the stars recede from one another, the effective wind velocity for both stars is reduced, which encourages the formation of thermal instabilities. Furthermore, as the OB star dominates the orbital dynamics of the system, the effective WR wind velocity is even further reduced, leading to an increased wind velocity ratio, resulting in a velocity shear that can drive KH instabilities.

There is much additional research potential in simulating dust growth in episodic WCd systems. Further simulations of this system in particular would involve simulating a full orbit, through the use of AMR and increased computing time. Other avenues of research include the effect on dust formation due to the influence of radiative line driving and sudden braking, as well as a more complex, multi-fluid dust model where dust grains are not explicitly coupled to the stellar wind.

6 ACKNOWLEDGEMENTS

REFERENCES

Callingham J. R., Tuthill P. G., Pope B. J. S., Williams P. M., Crowther P. A., Edwards M., Norris B., Kedziora-Chudczer L., 2019, Nature Astronomy, 3, 82
Castor J. I., Abbott D. C., Klein R. I., 1975, The Astrophysical Journal, 195, 157
Crowther P. A., 2003, Astrophysics and Space Science, 285, 677
Draine B. T., Salpeter E. E., 1979, The Astrophysical Journal, 231, 77
Dwek E., Werner M. W., 1981, The Astrophysical Journal, 248, 138
Dwek E., Foster S. M., Vancura O., 1996, The Astrophysical Journal, 457, 244
Eichler D., Usov V., 1993, The Astrophysical Journal, 402, 271
Gayley K. G., Owocki S. P., Cranmer S. R., 1997, ApJ, 475, 786
Hendrix T., Keppens R., van Marle A. J., Camps P., Baes M., Meliani Z., 2016, Monthly Notices of the Royal Astronomical Society, 460, 3975
Lamers H. J., Cassinelli J. P., 1999, Introduction to Stellar Winds. Cambridge University Press
Lau R. M., Eldridge J. J., Hankins M. J., Lamberts A., Sakon I., Williams P. M., 2020, ApJ, 898, 74
Monnier J. D., Tuthill P. G., Danchi W. C., 1999, ApJ, 525, L97
Monnier J. D., Tuthill P. G., Danchi W. C., Murphy N., Harries T. J., 2007, ApJ, 655, 1033
Pittard J. M., Dawson B., 2018, Mon Not R Astron Soc, 477, 5640
Prilutskii O. F., Usov V. V., 1976, Soviet Astronomy, 20, 2
Rosslowe C. K., Crowther P. A., 2015, Monthly Notices of the Royal Astronomical Society, 447, 2322
Ruuth S. J., Spiteri R. J., 2005, SIAM Journal on Numerical Analysis, 42, 974
Soulain A., et al., 2018, A&A, 618, A108
Spitzer L., 2008, Physical Processes in the Interstellar Medium. John Wiley & Sons
Stevens I. R., Pollock A. M. T., 1994, Mon Not R Astron Soc, 269, 226
Stevens I. R., Blondin J. M., Pollock A. M. T., 1992, The Astrophysical Journal, 386, 265
Stone J. M., Tomida K., White C. J., Felker K. G., 2020, ApJS, 249, 4
Thomas J. D., et al., 2021, Monthly Notices of the Royal Astronomical Society, 504, 5221
Tielens A. G. G. M., McKee C. F., Seab C. G., Hollenbach D. J., 1994, The Astrophysical Journal, 431, 321
Tuthill P. G., Monnier J. D., Danchi W. C., 1999, Nature, 398, 487
Williams P. M., van der Hucht K. A., Thé P. S., 1987, Astronomy and Astrophysics, 182, 91
Williams P. M., van der Hucht K. A., Pollock A. M. T., 1990, Monthly Notices of the Royal Astronomical Society, 243, 662
Williams P. M., et al., 2009, Monthly Notices of the Royal Astronomical Society, 395, 1749
Williams P. M., Crowther P. A., van der Hucht K. A., 2015, Monthly Notices of the Royal Astronomical Society, 449, 1834

This paper has been typeset from a TEX/LATEX file prepared by the author.